X-ray Absorption Spectroscopy and Reactivity of Thiolate-Ligated Fe-III-OOR Complexes

8 **AUTHORS**, INCLUDING:

Courtney M Krest
Stanford University
10 PUBLICATIONS   **258** CITATIONS

SEE PROFILE

James Penner-Hahn
University of Michigan
272 PUBLICATIONS   **10,069** CITATIONS

SEE PROFILE

David P Goldberg
Johns Hopkins University
81 PUBLICATIONS   **2,199** CITATIONS

SEE PROFILE

X-ray Absorption Spectroscopy and Reactivity of Thiolate-Ligated Fe^{III}-OOR Complexes

Jay Stasser[‡], **Frances Namuswe**[†], **Gary D. Kasper**[†], **Yunbo Jiang**[†], **Courtney M. Krest**[§], **Michael T. Green**[§], **James Penner-Hahn**[*,‡], and **David P. Goldberg**[*,†]

[†]Department of Chemistry, Johns Hopkins University, Baltimore, Maryland 21218

[‡]Department of Chemistry, University of Michigan, Ann Arbor, Michigan 48109

[§]Department of Chemistry, Pennsylvania State University, University Park, Pennsylvania 16802

Abstract

The reaction of a series of thiolate-ligated iron(II) complexes [Fe^{II}([15]aneN$_4$)(SC$_6$H$_5$)]BF$_4$ (**1**), [Fe^{II}([15]aneN$_4$)(SC$_6$H$_4$-*p*-Cl)]BF$_4$ (**2**), and [Fe^{II}([15]aneN$_4$)(SC$_6$H$_4$-*p*-NO$_2$)]BF$_4$ (**3**) with alkylhydroperoxides at low temperature (−78 °C or −40 °C) leads to the metastable alkylperoxo-iron(III) species [Fe^{III}([15]aneN$_4$)(SC$_6$H$_5$)(OOtBu)]BF$_4$ (**1a**), [Fe^{III}([15]aneN$_4$)(SC$_6$H$_4$-*p*-Cl)(OOtBu)]BF$_4$ (**2a**), and [Fe^{III}([15]aneN$_4$)(SC$_6$H$_4$-*p*-NO$_2$)(OOtBu)]BF$_4$ (**3a**), respectively. X-ray absorption spectroscopic studies (XAS) were conducted on the Fe^{III}-OOR complexes and their iron(II) precursors. The edge energy for the iron(II) complexes (~7118 eV) shifts to higher energy upon oxidation by ROOH, and the resulting edge energies for the Fe^{III}-OOR species range from 7121 – 7125 eV and correlate with the nature of the thiolate donor. EXAFS analysis of the iron(II) complexes **1 – 3** in CH$_2$Cl$_2$ show that their solid state structures remain intact in solution. The EXAFS data on **1a – 3a** confirm their proposed structures as mononuclear, 6-coordinate Fe^{III}-OOR complexes with 4N and 1S donors completing the coordination sphere. The Fe-O bond distances obtained from EXAFS for **1a – 3a** are 1.82 – 1.85 Å, significantly longer than other low-spin Fe^{III}-OOR complexes. The Fe-O distances correlate with the nature of the thiolate donor, in agreement with the previous trends observed for ν(Fe-O) from resonance Raman (RR) spectroscopy, and supported by optimized geometries obtained from density functional theory (DFT) calculations. Reactivity and kinetic studies on **1a – 3a** show an important influence of the thiolate donor.

Introduction

The coordination and processing of dioxygen and its reduced forms (superoxide, peroxide) at both heme and nonheme iron centers is of critical importance to a number of biological systems. These systems include the mononuclear nonheme iron enzymes superoxide reductase,[1-11] soybean lipoxygenase,[12] extradiol[13-16] and Rieske dioxygenases,[13,15,16] 1-aminocyclopropane-1-carboxylate oxidase,[17] and the antibiotic bleomycin.[16,18,19] Significant effort has gone into characterizing iron-dioxygen adducts (Fe-OO(H or R)) in both the biological systems and in biologically relevant small-molecule model complexes. However, structural characterization of such species remains limited. The first X-ray structure of a mononuclear nonheme iron-peroxide complex of any type appeared in 2001 with the crystallographic characterization of an alkylperoxo-iron(III) moiety in soybean

[*]dpg@jhu.edu, jeph@umich.edu .

lipoxygenase.[20] Other mononuclear, nonheme iron-peroxide adducts in proteins that have been crystallographically characterized include naphthalene dioxygenase (peroxo-iron),[21] homoprotocatechuate 2,3-dioxygenase (superoxo-, peroxo-, and alkylperoxo-iron)[14,15] and superoxide reductase (SOR) (peroxo-iron).[2] Given the paucity of structures available for these biologically relevant iron centers, it is important to obtain structural information on analogous model complexes, although thus far there is no X-ray structure available for a mononuclear nonheme iron-peroxide model complex. However, X-ray absorption spectroscopy (XAS) has been successfully employed to gain structural insights into such model complexes. For example, Kovacs has characterized a rare example of a thiolate-ligated, Fe^{III}-OOH complex by XAS,[22] and Que and coworkers have characterized both high-spin and low-spin nonheme alkylperoxo-iron(III) intermediates with various polydentate supporting ligands, mostly derived from pyridyl and/or neutral amine N donors.[23-25]

We have been successful in synthesizing a series of (N_4S(thiolate))iron(II) complexes and using them to generate metastable, low-spin alkylperoxo-iron(III) intermediates. These complexes were prepared as models of the reduced (His_4Cys)Fe^{II} SOR active site and (hydro)peroxo-iron(III) intermediates that may be important during turnover. SOR reduces superoxide to hydrogen peroxide as part of a natural defense mechanism in anaerobic microorganisms, and evidence suggests that a (hydro)peroxo-iron(III) intermediate may form during turnover. This intermediate must decay through Fe-O bond cleavage to release H_2O_2, and avoid O-O bond cleavage to give unwanted ferryl-type (Fe(O)) species.

In our earlier work the Fe^{III}-OOR model complexes were generated at low temperature (−78 °C) and characterized by UV-vis, EPR, and resonance Raman (RR) spectroscopies. Based on the combined spectroscopic data, these species were formulated as [Fe^{III}([15]aneN_4) (SC_6H_4-p-X)(OOR)]BF_4([15]aneN_4 = 1,4,8,12-tetraazocyclopentadecane; X = H, OMe, Cl, NO_2 or a polyfluorinated substituent; R = t-butyl or cumenyl), with a low-spin ferric center.[26,27] These low-spin Fe^{III}-OOR complexes contained arylthiolate ligands of varying electron-donating power, which allowed us to examine the influence of the sulfur donor on the spectroscopic properties of an Fe^{III}-OOR species at parity of ligand environment. Recently, we have also succeeded in probing the influence of the N donors of the [15]aneN_4 ligand, which led to the characterization of some *high-spin* Fe^{III}-OOR species.[28] The vibrational data from RR spectroscopy on the former series of low-spin Fe^{III}-OOR species showed that the identity of the thiolate ligand influences the strength of the Fe-O stretching frequency (ν(Fe-O)), but does not perturb the O-O vibration. As the thiolate becomes more electron-donating, a weakening of ν(Fe-O) is observed, consistent with a *trans* influence of the thiolate donor weakening the Fe-O bond. These findings were relevant to the proposed mechanism for SOR, which relies upon Fe-O bond cleavage of the (hydro)peroxo intermediate. However, concrete structural information on the Fe^{III}-OOR complexes was lacking.

Herein we have used X-ray absorption spectroscopy (XAS) to structurally characterize these complexes. Iron K-edge X-ray absorption spectra have been obtained for six different complexes, the alkylperoxo species [Fe^{III}([15]aneN_4)(SC_6H_5)(OOtBu)]BF_4 (**1a**), [Fe^{III}([15]aneN_4)(SC_6H_4-p-Cl)(OOtBu)]BF_4 (**2a**), and [Fe^{III}([15]aneN_4)(SC_6H_4-p-NO_2) (OOtBu)]BF_4 (**3a**), and the iron(II) precursor complexes [Fe^{II}([15]aneN_4)(SC_6H_5)]BF_4 (**1**), [Fe^{II}([15]aneN_4)(SC_6H_4-p-Cl)]BF_4 (**2**), and [Fe^{II}([15]aneN_4)(SC_6H_4-p-NO_2)]BF_4 (**3**). Examination of the XANES and EXAFS regions of the spectra has provided detailed structural information on both the iron(II) and alkylperoxo-iron(III) complexes, including confirmation of the thiolate ligation in both systems in solution. These studies have also led to insights regarding the influence of the thiolate donor on the structures of the alkylperoxo species. Comparison with the limited structural information on Fe^{III}-OOR(H) complexes

aids in our understanding of the selection by Nature of ligand type for the generation of peroxo-iron species with particular properties. The reactivity of the Fe^{III}-OOR species toward electrophiles, nucleophiles, and proton donors has also been examined. Kinetic studies on the decay of the Fe^{III}-OOR species suggest a reactivity pattern controlled by the identity of the thiolate donor.

Experimental Section

General Procedures—All synthetic reactions were carried out under an atmosphere of N_2 or Ar using a drybox or standard schlenk techniques. Reagents were purchased from commercial vendors and used without further purification unless noted otherwise. Dichloromethane was purified via a Pure-Solv Solvent Purification System from Innovative Technology, Inc. All solvents were degassed by repeated cycles of freeze-pump-thaw and then stored in a drybox. *Tert*-butylhydroperoxide was purchased from Aldrich as an ~5.5 M solution in decane over molecular sieves. The concentration of tBuOOH was determined as previously described.[27] Cumene hydroperoxide (CmOOH) was purchased from Aldrich as an 88% solution in ether. The iron(II) complexes $[Fe^{II}([15]aneN_4)(SC_6H_5)]BF_4$ (**1**), $[Fe^{II}([15]aneN_4)(SC_6H_4-p\text{-}Cl)]BF_4$ (**2**), and $[Fe^{II}([15]aneN_4)(SC_6H_4-p\text{-}NO_2)]BF_4$ (**3**) were synthesized according to published procedures.[27]

Physical Methods—Low-temperature UV-visible spectra were recorded at −78 °C or −40 °C (for kinetics) on a Cary 50 Bio spectrophotometer equipped with a fiber-optic coupler (Varian) and a fiber-optic dip probe (Hellma 661.302-QX-UV, 2 mm path length) for low temperature, using custom-made schlenk tubes designed for the fiber-optic dip probe. GC-FID analysis was performed on an Agilent 6890N GC equipped with a 30 m, 5% DPS column and an FID detector. GC-MS analysis was performed on a Shimadzu GC17A GC equipped with a 30 m, 5% DPS column and a QP5050A quadrupole MS detector.

Computational Methods—DFT calculations were performed on a model of the Fe^{III}-OOR complexes **1a** – **3a** in which R = CH_3. Frequency calculations were performed at optimized geometries. Initial coordinates were taken from the X-ray crystal structures of the iron(II) complexes **1** – **3**, and both high-spin and low-spin iron(III) configurations (S = 5/2 or 1/2) were evaluated. Calculations were performed with Gaussian 03 at the B3LYP/ 6-311G level of theory.[29]

XAS Sample Preparation—Custom designed sample holders consisted of an aluminum plate sealed with Kapton tape on both sides. Solid samples of **1, 2,** and **3** were prepared by mixing 5-10 mg of the Fe^{II} complexes with boron nitride under an inert gas atmosphere. The solid mixture was then transferred to an aluminum sample plate taped on one side. Sample preparation was completed by sealing the open side of the plate with Kapton tape. Samples of the alkylperoxoiron(III) complexes **1a, 2a** and **3a** were generated by adding 200 μL of the respective iron(II) precursors dissolved in CH_2Cl_2 (20 mM) to an aluminum sample holder sealed with Kapton tape on both sides with a volume capacity of 300 μL. The holders were cooled to −78 °C over dry ice, and then 50 μL of tBuOOH (1.75 equiv) stock solution in CH_2Cl_2 was added to each sample holder. The samples were mixed by manually shaking them, and after a suitable reaction time the desired chromophore was observed (~ 5 min). The samples were then immediately submerged in liquid nitrogen for storage until XAS studies could be conducted.

X-ray Absorption Spectroscopy. Data Collection and Analysis—Fe K-edge X-ray absorption spectra (XAS) were collected at the Stanford Synchrotron Radiation Laboratory (SSRL) on beamline 9-3 at 3 GeV with currents between 80 and 100 mA. The samples were kept at 10 K to 12 K in an Oxford liquid helium flow cryostat. Contamination of higher

harmonics radiation was minimized using a Rh-coated mirror upstream of the Si[220] double crystal monochromator; the mirror was set to a 10 keV energy cutoff. Data were collected in fluorescence excitation mode using a high-count-rate Canberra 30-element Ge array detector with maximum count rates held below 120 kHz per channel. Fe K-edge spectra were collected using 5 eV steps in the pre-edge (6900–7100 eV), 0.2 eV steps from 7100-7140 and 0.05 Å^{-1} steps in the EXAFS region to k = 15 Å^{-1}. Data collection was integrated for 1s in the preedge, 1.5 s in edge regions, and 1.5 to 25 s (k^2-weighted for k = 2.6 to 8 Å^{-1} and k^3-weighted for k = 8 to 15 Å^{-1}) in the EXAFS region for total scan time of roughly 45 min. A Mn filter (absorption equivalent to ~20 μm Mn metal) was placed in front of the detector to reduce the elastic scatter peak and Soller slits were used to reduce the Mn $K_α$ fluorescence. Each sample was scanned multiple times to give a total of ~10^9 counts total in the windowed Fe $K_α$ peak at k = 15 Å^{-1}, requiring 3 to 10 scans depending on sample concentration.

X-ray energies were calibrated by simultaneous measurement of a Fe foil absorption spectrum and assigning the first inflection point of the absorption edge as 7111.2 eV. Data from each detector channel were inspected for glitches before inclusion in the final average. Pre-edge subtraction and normalization to McMaster values[30] were carried out using the program MBACK.[31] A four-region third-order polynomial spline was fit over the range of the data and subtracted to give the final EXAFS spectrum by using EXAFSPAK, made available by Dr. G. George on the SSRL Web site. The data were converted to k space via the equation:

$$k = \left[2m_e \left(E - E_0 \right) / h^2 \right]^{1/2}$$

where E_0 = 7112 eV. Data were fit, using Excurv98,[32] to the EXAFS equation:

$$\chi(k) = \sum_s \frac{N_s A_{as}(k)}{kR_{as}^2} \exp\left(-2\sigma_{as}^2 k^2\right) \sin\left[2kR_{as} + \phi_{as}(k)\right]$$

where N_s is the number of scatterers with atom type s at a distance of R_{as}. $A_{as}(k)$ is the effective back-scattering amplitude function, σ^2_{as} is the Debye-Waller factor and $\sigma_{as}(k)$ is the phase shift of the photoelectron wave traveling between the potentials of the absorbing and scattering atoms. Fourier transforms of the EXAFS data were calculated using k^3-weighted data from k = 2.0-15 Å^{-1}. Multiple scattering paths, phase shifts, and amplitudes were calculated in the Excurv98 program. Data were k^3-weighted and the individual fits were performed with the coordination numbers fixed and the Debye-Waller factors held constant at values suggested by Dimakis and Bunker,[33] while the R_{as} values were allowed to vary. This fitting process allowed us to determine coordination number and R_{as} values with a minimal number of parameters. After obtaining optimal fits in this manner, the Debye-Waller factors were varied and shown to refine to reasonable values. Distances of the outer shell carbons in both the N_4 and S donors were initially set using the crystallographic distances. Fits were constrained to have fixed S-C, N-C, and C-C distances, but were allowed to have freely variable angles between the metal center and the ligand, for a total of 8 variable parameters each for the thiolate and the macrocyclic N_4 ligand. In addition to the variable distances, the threshold energies were allowed to vary. The final structures were analyzed to insure that in no case were there significant changes in the intramolecular angles. In addition (see below) the Fe-O and Fe-S coordination numbers were varied for some fits.

Pre-edge peaks were isolated by fitting the edge and first XANES peak (7100 – 7150 eV) background using the sum of an arctan + Gaussian functions. This background was then subtracted from the normalized data to isolate the pre-edge peak.

Reaction of Alkylperoxo-Iron(II) Complexes with Electrophiles and Nucleophiles—The compounds PPh$_3$, cyclooctene, 2,6-di-*t*-butylphenol, cyclohexadiene (CHD), 2-phenyl propionaldehyde (2-PPA), cyclohexane carboxaldehyde (CCA), and H$^+$BF$_4$$^-$·Et$_2$O were reacted with the alkylperoxo-iron(III) complexes generated *in situ* by similar methods. In a typical reaction, a solution of **1** in CH$_2$Cl$_2$ (7 mL, 3.31 mM) was cooled to −78 °C, and tBuOOH (101 μL, 5.79 mM) was added from a stock solution in decane/CH$_2$Cl$_2$. An immediate color change from colorless to dark red was noted. The reaction was allowed to stir until the alkylperoxo-iron(III) species **1a** was fully formed, as indicated by maximal absorbance at 526 nm. The substrate 2-PPA (922 μL, 200 equiv.) was then added, and caution was taken to prevent warming of the reaction mixture. A rapid color change from red to yellow was observed. After the red color was completely discharged, the reaction mixture was warmed to room temperature and analyzed by GC-FID.

Kinetic Studies—In a typical reaction, [Fe^{II}([15]aneN$_4$)(SC$_6$H$_4$-*p*-X)]BF$_4$ (X = H, Cl, NO$_2$) (5 – 10 mg) was loaded in a Schlenk flask and dissolved in CH$_2$Cl$_2$ to give a final concentration of 1 - 3 mM. A fiber optic dip-probe for UV-vis measurements was inserted into the flask and the solution was cooled to −40 °C. The alkylhydroperoxide (tBuOOH or CmOOH, 1.5 equiv, in CH$_2$Cl$_2$) was added to the Fe^{II} complex. A color change from colorless (yellow for **3**) to burgundy was observed, indicating the formation of **1a – 3a** or **1b** – **3b**, which was confirmed by UV-vis. The kinetics of decay of the alkylperoxo-iron(III) species was monitored by UV-Vis spectral changes at 529, 524, 522, 528, 530, 521 nm. Isosbestic points were observed throughout the decay of each complex. First-order rate constants (k_{obs}) were calculated by plotting ln[(A$_t$-A$_f$)/(A$_0$-A$_f$)] vs time, where A$_0$ = initial absorbance at time = 0, A$_t$ = absorbance at time *t*, and A$_f$ = final absorbance. Kinetic data for each intermediate were collected at least in triplicate.

Results and Discussion

Preparation of the Alkylperoxo Complexes [Fe^{III}([15]aneN$_4$)(SC$_6$H$_4$-*p*-X)(OOtBu)]$^+$

The alkylperoxo-iron(III) complexes [Fe^{III}([15]aneN$_4$)(SC$_6$H$_5$)(OOtBu)]BF$_4$ (**1a**), [Fe^{III}([15]aneN$_4$)(SC$_6$H$_4$-*p*-Cl)(OOtBu)]BF$_4$ (**2a**), and [Fe^{III}([15]aneN$_4$)(SC$_6$H$_4$-*p*-NO$_2$) (OOtBu)]BF$_4$ (**3a**) were generated by addition of tBuOOH to their respective iron(II) precursors at low-temperature, as shown in Scheme 1. Previously these species, which are a dark burgundy in color, were characterized by UV-vis spectroscopy and exhibited UV-vis bands between 520 – 530 nm, which are indicative of an alkylperoxo-to-iron(III) LMCT band. Resonance Raman spectroscopy confirmed their identities as alkylperoxo complexes, with prominent peaks between 610 – 620 cm^{-1} typical of ν(Fe-O) and a peak near 800 cm^{-1} characteristic of ν(O-O), both of which shifted with ^{18}O substitution. These complexes were characterized as low-spin Fe^{III} (S = ½) by EPR spectroscopy. The analogous series of alkylperoxo complexes **1b** – **3b** were prepared in the same manner (Scheme 1) and exhibited similar spectroscopic signatures in the UV-vis, RR, and EPR measurements.[27] However, direct characterization of the solution state structures of either the iron(II) precursor complexes or the alkylperoxo-iron(III) species were lacking. Below we describe XAS studies aimed at obtaining detailed structural information of these complexes.

X-ray Absorption Near-Edge Spectroscopy (XANES) of the Fe[II] complexes and Fe[III]-OOtBu Intermediates

The X-ray absorption spectra in the near-edge region for the iron(II) precursor complex **1** as a crystalline solid (dispersed in boron nitride (BN) matrix) and dissolved in solution (CH_2Cl_2) are shown in Figure 1, and similar plots for **2** and **3** are given in Figure S1. The solution state data for all three Fe[II] complexes **1** – **3** are overlayed for comparison in Figure 2. The energy of the rising Fe K-edge depends both on the metal oxidation state and on the structure. In particular, a decrease in Fe-ligand distance (for example, because of a change in coordination number or a change in spin state) typically results in an increase in edge energy. The edge energy for crystalline **1** is 7116.9 eV, and falls in the expected range for an iron(II) complex.[22,34] The edge is shifted to higher energy by ~1.1 eV upon dissolution of the complex in CH_2Cl_2, and the intensities of the first two XANES peaks (~7130-7135 eV) are altered, with the second peak going from a weak, poorly resolved shoulder to a pronounced peak. Nearly identical changes are seen for **2** and **3** (Figure S1). These data demonstrate that a structural rearrangement of some sort takes place for **1** – **3** upon dissolution, although it is difficult to interpret the higher energy XANES features, which are sensitive to small changes in multiple scattering, in terms of quantitative structural changes. While it is possible that changes such as these could arise from partial oxidation of Fe[II] to Fe[III] (complete oxidation would induce a much larger shift, see the spectrum for **1a** in Figure 1 for comparison), careful observation of the color of the samples (colorless for Fe[II], brown upon conversion to Fe[III] by exposure to air) showed no evidence of oxidation. Similarly, the XANES changes on dissolution (Figs. 1 and S1) could, in principle, arise from gross decomposition of the complex; however, this possibility can be excluded by the EXAFS results (vide infra) demonstrating that the core ligation remains unchanged, aside from modest changes in bond length.

For comparison, the near-edge regions for **1** – **3** in CH_2Cl_2 are plotted together in Figure 2. The shape and position of the rising edge for all three compounds are nearly identical (edge energy = 7117.9 eV (**1**); 7118.1 eV (**2**); 7118.0 eV (**3**)), and all three show broad, weak pre-edge transitions at ~7111 eV (inset, Figure 2). Thus it is unreasonable to assume that the modest changes in the edge regions of **1** – **3** upon dissolution arise from identical amounts of air contamination and subsequent oxidation, but rather these changes must arise from conformational changes of the complexes. The pre-edge peaks appear to arise from several overlapping peaks, which can be assigned to formally parity-forbidden $1s \rightarrow 3d$ transitions. From the crystallographic data on these high-spin iron(II) complexes, the iron centers are best described as distorted square pyramidal based on a normalized τ value[35] ($\tau = 0.50$ (**1**), 0.50 (**2**), 0.27 (**3**), where $\tau = 0$ for trigonal bipyramidal and $\tau = 1.0$ for square pyramidal). The overlapping peaks observed in the pre-edge region can be attributed to the multiple $1s \rightarrow 3d$ transitions that are available for 5-coordinate, high-spin Fe[II], which contains up to four "holes" in the d shell with differing energies.[34]

The near-edge regions of the XANES spectra for the low-spin iron(III)-alkylperoxo complexes **1a** – **3a** are shown in Figure 3, and they are also overlayed against their reduced iron(II) precursors in Figures 1 and S1 for comparison. The Fe K-edge energies for **1a** – **3a** are upshifted by 3 – 7 eV as compared to the iron(II) precursors **1** – **3**. This increase in edge energy is consistent with an increase in oxidation state from Fe[II] to Fe[III] for **1a** – **3a**. Although the edge positions for **1a** – **3a** vary by ~ 3 eV, they all fall in the range as previously reported Fe[III]-OOR(H) complexes,[22-24,36-41] Given that **1a** – **3a** are all Fe[III] complexes, the change in the edge energies must arise either from differences in the coordination environments of the metal centers, from differences in composition (e.g., partial decomposition), or from a combination of these effects. Inspection of the trend in edge energies for **1a** – **3a** reveals that they correlate with the identity of the thiolate donor, decreasing as the thiolate ligand becomes less electron-donating (**1a**: 7124.6 eV > **2a**:

7122.4 eV > **3a**: 7121.4 eV). A reduction in the edge energy can be attributed to a strengthening of the Fe-O bond, which satisfyingly corroborates our previous analysis.[26,27] In our earlier work, it was shown that the Fe-O stretching frequency increases as the thiolate ligand becomes a weaker donor (ν(Fe-O): **1a** < **2a** < **3a**), which was interpreted as a strengthening of the Fe-O bond induced by a reduction of the *trans* effect of the thiolate ligand. A similar shift in edge energies was reported for a pair of high-spin Fe^{III}-OOtBu complexes $[Fe^{III}(L^8Py_2)(OOtBu)(X)]^{2+}$ (L^8Py_2 = 1,5-bis(pyridin-2-ylmethyl)-1,5-diazacyclooctane, X = CH_3CN or pyridine *N*-oxide (PyO)), in which the more weakly donating CH_3CN ligand resulted in a 2.1 eV downshift of the edge position. This result was attributed to an increased covalency of the Fe^{III}-OOR bond for the CH_3CN complex.[25] Thus, the XANES data for **1a** – **3a** provide good evidence that the covalency, and therefore the bond strength, of the Fe-O bonds in these complexes is directly influenced by the nature of the thiolate ligand.

Expanded views of the pre-edge regions for **1a** – **3a** (Figure 3), show the 1s → 3d transitions. The pre-edge features for **1a** and **2a** are similar in energy and intensity, while that for **3a** appears to be shifted to lower energy by ~1 eV and to be more intense. This apparently anomalous behavior for **3a** is, at least in part, the consequence of the fact that the XANES spectrum for complex **3a** appears to have a significantly different background. Thus, once the background is subtracted, it is clear that 1s-3d transitions (Fig. 4) all occur at approximately the same energy. The pre-edge peaks for **1a** and **2a** are less intense than those observed for the iron(II) precursor complexes. This result is consistent with the iron centers of **1a** and **2a** being 6-coordinate, compared to the 5-coordinate environments of the iron centers in **1** and **2** since, in general, 1s-3d intensity decreases as coordination number increases, due to the fact that the metal has become more nearly centrosymmetric.[34,42] Interestingly, the pre-edge feature for the *para*-nitro complex **3a** appears more intense than its iron(II) precursor. While this may be due, in part, to an increase in the strength of the Fe-O interaction (see below), it may also reflect incomplete background removal in this case. A stronger Fe-O interaction would reduce the symmetry of the iron site and cause a gain in intensity of the pre-edge features. This result also correlates with the trend in Fe-O bond distances seen by EXAFS (*vide infra*).

EXAFS Spectra and Fitting Results. Iron(II) Complexes

The normalized, phase-shifted Fourier transforms (FT) of the Fe K-edge EXAFS data and the EXAFS spectra (insets) for the three high-spin, thiolate-ligated iron(II) precursor complexes **1** – **3** in frozen CH_2Cl_2 solution are shown in Figure 5. The best fits are overlaid with the spectra, and the curve-fitting results are summarized in Table 1. The analogous data for **1** – **3** in the solid state are presented in Figure S3 and Table S1. The most prominent feature in the Fourier transforms for all three complexes in CH_2Cl_2 is a peak with a maximum at R ~ 2.1 Å. There is also a broad peak of significant intensity at R ~ 3.0 Å. The fitting of the EXAFS data for **1** – **3** are all similar and therefore only the fitting for **1** is described here in detail. The best fit includes a combination of four nitrogen/oxygen scatterers and a single sulfur scatterer attached to the Fe^{II} center. In fits 1 and 2 in Table 1, the Debye-Waller factors were fixed so as to determine the importance of inclusion of the sulfur scatterer. Clearly, the single sulfur scatterer is necessary for a good fit. Debye-Waller factors were then refined to reasonable values, as seen in fit 3 (best fit, bold). The fitted model corresponds to that expected from XRD, with four nitrogen donors from the [15]aneN_4 ligand and the sulfur donor from the phenylthiolate ligand comprising the first coordination sphere around the metal. Fitting of the outer-sphere features was accomplished with the addition of 2 carbon shells: 1 C scatterer at 3.43 Å and 2 C scatterers at 4.16 Å, attributed to the C atoms of the phenylthiolate ligand in proximity to the S donor. In addition, shells of 8 C atoms at 2.96 Å and 3 C atoms at 3.26 Å were included and attributed

to the N-<u>C</u> and N-C-<u>C</u> atoms, respectively, of the [15]aneN$_4$ ligand. Inclusion of these outer-sphere shells, in which multiple scattering paths were included, led to a significant improvement in the fit quality (i.e., the F index) as compared to fits that included only single scattering shells.

The Fe-S distances from the EXAFS for **1 – 3** in CH$_2$Cl$_2$ solution are close to those found by XRD (2.3197(12) – 2.3316(11)Å), but the average Fe-N distances appear shorter by EXAFS (XRD: Fe-N$_{ave}$ = 2.109 – 2.195 Å). The best fits of the EXAFS for the crystalline samples for **1 – 3** (Table S1) also yield Fe-N$_{ave}$ distances (2.06 – 2.12 Å) that are somewhat shorter than those found by XRD. Although the EXAFS data for both the solution state and solid state samples can only be fit with N$_4$S ligation, the EXAFS-derived distances are significantly shorter in solution (0.02-0.04 Å for Fe-N, 0.05-0.07 Å for Fe-S). The origin of this discrepancy is not known. In any case, the EXAFS corroborates the findings from the XANES, which indicate that there is a structural rearrangement for the Fe^{II} complexes upon dissolution. Attempts to fit the solution state EXAFS in Figure 5 with a sixth low Z scatterer at bonding distance to the iron, such as a weakly bonded BF$_4^-$ anion or exogenous solvent molecule (e.g. H$_2$O), led to poor agreement with the data and unreasonably high Debye-Waller factors. Taken together, the EXAFS spectra for **1 – 3** are in full agreement with these complexes being 5-coordinate, and confirm that the 4N/1S coordination sphere remains intact in solution.

Alkylperoxo-Iron(III) Complexes

The EXAFS spectra for the three *t*-butylperoxo-iron(III) complexes **1a** – **3a** together with the best fits are shown in Figure 6, and the fitted parameters are given in Table 2. Fitting results were similar for **1a** – **3a**, so only **1a** will be discussed in detail. There are three prominent peaks apparent in the Fourier-transformed data at $R \sim$ 1.9, 2.1 and 3.0 Å. The main difference in the Fourier-transforms of the EXAFS for **1a** – **3a,** as compared to their iron(II) precursors, is the additional short shell near 1.9 Å, which is attributed to the addition of the t-butylperoxo ligand. Accordingly, the best fits to the data for **1a** – **3a** require 3 shells of scatterers consisting of one N/O scatterer at 1.82 – 1.85 Å, 4 N/O scatterers at 2.06 – 2.10 Å, and one sulfur scatterer at 2.29 – 2.32 Å. The innermost shell can be attributed to the O atom of the alkylperoxo ligand, while the next shell corresponds to the four nitrogen atoms of the macrocyclic [15]aneN$_4$ ligand in **1a** – **3a**. The S donors from each of the arylthiolate ligands make up the third shell. Attempts were made to fit the data in the absence of the sixth S donor (Table 2, fit 1), in the absence of the alkylperoxo ligand (Table 2, fit 2), or with a lower Z scatterer (N/O) in the sixth position (Table 2, fit 3), but in all of these cases this gave a worse fit. Slight improvements to the fit (~2% decrease in F) were seen if the population of the S scatterer was allowed to vary between 0.5 – 1.0. Less than full occupancy of the S donor can be expected given the likelihood of minor decay of these species during sample preparation because of their extreme thermal instability. Similar modest improvements to the fit were seen upon allowing the O atom occupancy at ~1.85 Å to vary, also consistent with possible minor decomposition of **1a** ((compare Table 2, fits 4 and 5). Although the EXAFS data were measured to relatively high resolution, it is difficult, in general, to reliably fit three independent shells of nearest neighbors due to the possibility of interference between the different scattering shells. Thus, the observation that the bond lengths are unchanged when the Fe-O and Fe-S coordination numbers are allowed to vary (compare fits 4 and 5) provides additional evidence that all 3 shells are required. Only for **3a** is there a significant decrease in the refined Fe-O coordination number, consistent with the suggestion from the XANES that this complex may be slightly decomposed.

The inclusion of outer-sphere carbon shells led to a further improvement of the fit. As found for **1 – 3**, the number and distance of the outer-sphere C scatterers correspond to the carbon atoms closest to the N and S donors. For all three complexes, the Debye-Waller factors were

allowed to vary after optimizing the fit for coordination number, type of scatterer, and R_{as} values as described above. As seen in the best fits 6-8, the Debye-Waller factors refine nicely to reasonable values. Overall, it is evident that EXAFS data for the three alkylperoxo complexes **1a** – **3a** require the presence of four nitrogen donors from the tetraazamacrocycle together with one oxygen and one sulfur donor, attributed to the alkylperoxo and thiolate ligands, respectively. Thus the EXAFS data are in excellent agreement with the proposed structures of **1a** – **3a** shown in Scheme 1.

The optimized geometries of the three Fe^{III}-OOR complexes were calculated previously by density functional theory (DFT),27 and the calculated iron-ligand bond distances are presented in Table 3 for comparison with the EXAFS data. The coordinates from the X-ray structures of the Fe^{II} precursors **1** – **3** were used as the initial models in the calculations, and the tBu group of the alkylperoxo ligand was truncated to a methyl substituent in order to facilitate the computations. The optimized structure for the PhS^- complex is shown in Figure 7. The ground spin state for all three complexes was found to be low-spin Fe^{III} ($S = \frac{1}{2}$), in agreement with the EPR analysis of **1a** – **3a**. As seen in Table 3, the average Fe-N distances obtained by EXAFS are close to those predicted by DFT. These Fe-N distances are slightly elongated in comparison to other low-spin Fe^{III} complexes, where d(Fe-N) is usually closer to 2.0 Å. Thus steric constraints on the [15]aneN_4 ligand may cause the Fe-N bonds to be slightly elongated in **1a** – **3a**. The Fe-O bond lengths from DFT and EXAFS are in excellent agreement, and the Fe-S distances calculated by DFT are also reasonably close to those derived from EXAFS, although the DFT distances are somewhat longer by 0.07 – 0.08 Å. Metal-ligand distances for longer, weaker bonds are often overestimated by DFT.43

Given the observed conformational change for the iron(II) complexes upon dissolution, it is worthwhile to consider the possibility of "folding" of the macrocycle in the alkylperoxo complexes, such that the alkylperoxo and thiolate ligands are positioned *cis* to each other. The [15]aneN_4 ligand exhibits only a *trans* geometry for all known trivalent metal complexes, unlike cyclam ([14]aneN_4), which can in fact fold into a *cis* geometry. Thus, given the spectroscopic data, trends in the EXAFS (vide infra), and DFT-optimized structures, we conclude that the alkylperoxo-iron(III) species are in a *trans* geometry. We have commented in some detail on this issue previously.27

An important finding from the EXAFS, and corroborated by the DFT calculations, is that the identity of the arylthiolate ligand influences both the Fe-S and Fe-O distances. As the *para* substituent of the arylthiolate becomes more electron-withdrawing, the Fe-S distance becomes longer (d(Fe-S): **3a** > **2a** > **1a**), consistent with the expected weakening of the Fe-S bond for a more electron-poor thiolate donor. The opposite pattern is seen for the Fe-O bond lengths measured by EXAFS (d(Fe-O): **1a** > **2a** > **3a**), which is also reflected in the DFT calculations. Although the changes in the EXAFS Fe-O distance are small (ΔFe-O = 0.03 Å) and close to the estimated accuracy of EXAFS (~0.02 Å), these differences are significantly greater than the precision of EXAFS (~0.004 Å), and are consistent with the magnitude of the changes predicted by the DFT calculations.

Previously some of us had described a correlation between the nature of the thiolate ligand and the Fe-O stretching frequency (ν(Fe-O)) obtained from RR spectroscopy for **1a** – **3a**.27 The ν(Fe-O) values of **1a** – **3a** are reproduced in Table 3 for comparison. Based on the vibrational data, it was suggested that the strength of the Fe-O bond increases as the thiolate ligand becomes a weaker donor. However, the ν(Fe-O) vibration for other Fe^{III}-OOR complexes has been shown to be coupled to other vibrational modes, preventing a staightforward connection of bond strengths with vibrational frequencies.25,37,44,45 For the Fe^{III}-OOR complexes described here, it was found that the isotopic shifts ($\Delta\nu$(Fe-^{16}O/^{18}O)) for the ^{18}O-labeled isotopomers matched those predicted for simple

diatomic oscillators, suggesting that a direct correlation could be made between their vibrational frequencies and bond strengths. In the present study we have demonstrated that the Fe-O distance, which is necessarily related to bond strength, correlates with the identity of the thiolate ligand as predicted by the vibrational data. Thus the EXAFS provides strong support for the conclusion that a weakening of the Fe-S interaction *trans* to the alkylperoxo ligand induces a concomitant strengthening of the Fe-O bond.

Further insight regarding the influence of a thiolate donor on the Fe-O interaction can be seen from a comparison with the limited metrical information available for other Fe^{III}-OOR complexes. The Fe-O distances found for **1a** – **3a** are significantly longer than almost all other low-spin Fe^{III}-OOR(H) complexes, which do not contain thiolate donors and display d(Fe-O) = 1.76 – 1.81 Å. The Fe-O distances for the *low-spin* alkylperoxo complexes **1a** – **3a** are closer to those recently reported for the *high-spin* Fe^{III}-OOR species (d(Fe-O) = 1.86 – 1.96 Å), where an elongation in metal-ligand distance is expected compared to their low-spin analogs.[25] The only other low-spin Fe^{III}-OOR(H) complex with a similar elongated Fe-O distance is the thiolate-ligated complex $[Fe^{III}(S^{Me2}N_4(tren)(OOH)]^+$, with d(Fe-O) = 1.86 Å derived from EXAFS.[22] Thus thiolate ligation appears to be critical for elongating and weakening the Fe-O bond in this complex as well as in **1a** – **3a**. Interestingly, the thiolate donor is held *cis* to the (hydro)peroxo ligand in $[Fe^{III}(S^{Me2}N_4(tren)(OOH)]^+$, in contrast to the proposed *trans* arrangement in **1a** – **3a**, suggesting that perhaps the presence of a strong anionic donor such as RS^- is the dominant factor in weakening the Fe-OOR(H) interaction, while its positioning to the peroxo binding site is of secondary importance. It should be noted that a mutant form of superoxide reductase, E114A-SOR, reacts with H_2O_2 to give an Fe^{III}-OO(H) adduct that has been characterized by XRD and exhibits an Fe-O distance of 2.0 Å,[2] in good agreement with the model complexes.

Reactivity of the Alkylperoxo-Iron(III) Species

Mononuclear nonheme iron-(hydro)peroxo and alkylperoxo complexes[40,46-50] have been investigated as both electrophilic and nucleophilic oxidants. The examination of such reactivity has helped in delineating the possible roles that such species might play in enzymatic or synthetic catalytic reactions. Given this motivation, we tested the reactivity of the alkylperoxo-iron(III) complexes toward organic substrates to determine if they could function as either electrophilic or nucleophilic oxidants (Scheme 2). The nucleophilic substrates PPh_3 and cyclooctene were added to **1a** at low temperature. These substrates are prone to oxidation by electrophilic metal-oxo species, giving $OPPh_3$ or cyclooctene oxide, respectively. The burgundy alkylperoxo complex **1a** was generated in the usual manner at low temperature, as seen by formation of the peak at λ_{max} 526 nm. After maximal formation of the peak at 526 nm, excess PPh_3 (~50 equiv) or cyclooctene (~100 equiv) dissolved in CH_2Cl_2 was added slowly to the reaction mixture at −78 °C, with care taken to avoid warming the solution. The addition of either substrate did not change the rate of self-decomposition of **1a**. The reaction mixtures were warmed to room temperature and analyzed by GC to determine if substrate oxidation occurs upon thermal decomposition of **1a**. One pathway for the decomposition of **1a** might involve O-O cleavage to give a high-valent iron-oxo species ($Fe^{IV}(O)$ or $Fe^{V}(O)$), which could potentially be intercepted by substrate to give oxygenated product(s). For both the PPh_3 and cyclooctene reactions, no oxidation products ($OPPh_3$ or cyclooctene oxide) were observed over the background reaction (substrate + tBuOOH, in the absence of Fe complex). Thus the alkylperoxo complex **1a** is unreactive toward these oxygen atom acceptors and does not seem to function as an electrophilic oxidant. These results further suggests that the thermal decomposition of **1a** does not proceed via a mechanism that leads to a significant build-up of a high-valent Fe(O) complex.

The chloro-substituted complex **2a** was employed to test possible reactivity toward H-atom donors. The alkylperoxo complex was generated at −78 °C as described above, and then the

H-atom donor 2,6-di-tert-butylphenol or cyclohexadiene (CHD) was added in excess (~50 equiv) (Scheme 2). The addition of these potential H-atom donor substrates did not cause a detectable increase in the rate of disappearance of **2a** at −78 °C as monitored by UV-vis. Reaction mixtures with CHD as substrate were warmed to room temperature and analyzed by GC, but the production of benzene was not observed. These data support the conclusion that the alkylperoxo complexes do not function as electrophilic oxidants, and furthermore, do not decompose in a way that leads to a build up of a reactive high-valent Fe(O) species.

It is known that heme and nonheme iron(III)-(hydro)peroxo complexes can function as nucleophilic oxidants toward electrophilic substrates such as aldehydes.[51,52] A recent, related example of such reactivity comes from a report on a structurally characterized *tert*-butylperoxo-nickel(II) complex, which reacts with CO and substituted benzaldehydes to yield a carbonato-bridged nickel dimer or the corresponding benzoato complex, respectively.[53] Interestingly, addition of 2-phenyl propionaldehyde (2-PPA) in excess (200 equiv) to **1a** at −78 °C resulted in an immediate color change from burgundy to yellow, accompanied by a loss of the peak for **1a** at 526 nm (Scheme 2). A similar rapid color change and loss of the 526 nm peak was seen upon addition of a second aldehyde substrate, cyclohexane carboxaldehyde (CCA). Thus the large increase in the rate of self-decomposition of **1a** with aldehyde substrates suggest a reaction is occuring with **1a** and these electrophilic substrates. However, analysis of reaction mixtures by GC did not reveal the expected deformylation products (acetophenone in the case of 2-PPA, or cyclohexenone in the case of CCA). These results suggest that the alkylperoxide of **1a** may function in a nucleophilic capacity toward aldehyde substrates, but the mechanism of substrate decomposition does not lead to deformylation products. We note that even in the case of heme- and non-heme (hydro)peroxo-iron species that lead to deformylation products, the mechanism of deformylation is not well understood. We also examined the reactivity of one of the alkylperoxo complexes toward proton donors (Scheme 2). The cumenylperoxo-iron(III) complex **1b** was treated with $H^+BF_4^- \cdot Et_2O$ (one equiv) at −78 °C, and the reaction was monitored by UV-vis in the usual manner. Upon injection of $H^+BF_4^-$ there was an immediate loss of the burgundy color and decrease at 528 nm, resulting in a final brown solution. This rapid acceleration of the self-decomposition of **1b** in the presence of H^+ is consistent with the the alkylperoxo species exhibiting nucleophilic character.

Decay kinetics

The decay kinetics of the alkylperoxo species **1a** – **3a** and **1b** – **3b** in CH_2Cl_2 at −78 °C are complicated and do not follow a simple first-order process. We therefore attempted to monitor the decay kinetics at a different temperature. Although the alkylperoxo-iron(III) species decompose rapidly upon warming from −78 °C to room temperature, we found that they could be generated at −40 °C and have sufficiently long enough lifetimes to allow us to monitor their decay by UV-vis spectroscopy. As can be seen in Figure 8, the disappearance of the six different alkylperoxo complexes **1a** – **3a** and **1b** – **3b** were monitored by following the decrease in the peaks between 519 – 530 nm. A smooth decay of these bands was observed, together with the concomitant loss of the red chromophore. The final spectrum in each case corresponds to yellow-brown reaction mixtures that contain unidentified iron(III) products. Significant efforts have been made to crystallize these final product(s), but we have been unable to obtain crystalline materials suitable for characterization by X-ray diffraction.

The natural log plots (insets, Figure 8) are linear to ~3 half-lives, with the exception of **3b**, which was monitored for ~1.5 half-lives. Thus the decay kinetics at −40 °C follow good first-order behavior, in contrast to what is seen at −78 °C, where the decay curves do not follow simple first-order behavior. These data suggest that there is one dominant decay pathway at −42 °C, whereas at −78 °C there may be competing mechanisms of decay. The

slopes of the best-fit lines of the natural log plots in Figure 8 yield first-order decay rate constants (k_{dec}) for each of the complexes as follows: $k_{dec} = 3.6(1) \times 10^{-2} s^{-1}$ (**1a**), $K_{dec} = 7.5(2) \times 10^{-3} s^{-1}$ (**2a**), $k_{dec} = 7(2) \times 10^{-3} s^{-1}$ (**3a**), $k_{dec} = 1.6(2) \times 10^{-2} s^{-1}$ (**1b**), $k_{dec} = 4.0(7) \times 10^{-3} s^{-1}$ (**2b**), and $k_{dec} = 2.0(3) \times 10^{-3} s^{-1}$ (**3b**). The rate constants for both the Fe^{III}-OOtBu and Fe^{III}-OOCm complexes follow a clear trend in relation to the nature of the thiolate ligand *trans* to the alkylperoxo moiety, showing that the alkylperoxo complexes are significantly stabilized as the *para* substituent on the thiolate ligand increases in its electron-withdrawing character. These effects are highlighted by comparing the half-life ($t_{1/2}$) of the most stable species **3b** ($t_{1/2} = 347$ s) which carries the *p*-NO$_2$-substituted thiolate, whereas the unsubstituted phenylthiolate ligand in **1a** exhibits $t_{1/2} = 43$ s. The trend observed for the rates of self-decomposition versus the identity of the thiolate ligand for both the *tert*-butylperoxo- and cumenylperoxo-iron(III) complexes is in excellent agreement with the vibrational data, EXAFS, and DFT calculations. Interestingly, a comparison of the rate constants between the *tert*-butylperoxo and cumenylperoxo complexes also exhibits a pattern that corresponds to our previous results from resonance Raman studies. The cumenylperoxo complexes exhibit higher energy Fe-O stretching frequencies than their *tert*-butylperoxo-iron(III) analogs (Fe-OOCm: ν(Fe-O) = 622 – 631 cm^{-1}; Fe-OOtBu: ν(Fe-O) = 608 – 623 cm^{-1}). The rates of decay for each of the cumenylperoxo complexes are slower than the corresponding *tert*-butylperoxo complexes, correlating nicely with the difference in ν(Fe-O).

There is limited information on the kinetics of decay of Fe^{III}-OOR species, but two important studies are relevant to the current work. The kinetics of decay for a low-spin Fe^{III}-OOtBu complex, [Fe^{III}(TPA)(OOtBu)(NCCH$_3$)]$^{2+}$ (TPA = *tris*(pyridyl-2-methyl)amine) was measured at −36 °C in CH$_3$CN and found to accelerate in the presence of Lewis bases such as 4-substituted pyridines and pyridine *N*-oxides. An enhanced effect was noted upon increasing the electron-donating ability of the added Lewis base.[49] The UV-vis spectral decay of the alkylperoxo complex was accompanied by the appearance of a spectrum indicative of an Fe^{IV}(O) complex, suggesting a decay mechanism involving homolytic cleavage of the O-O bond of the alkylperoxo ligand. Thus in this case the Lewis bases likely coordinate to the metal and facilitate O-O bond cleavage through a "push effect". In contrast, the rates of decay for a series of *high-spin* Fe^{III}-OOtBu complexes [Fe^{III}(L$_8$Py$_2$)(OOtBu)(X)]$^+$, where X = OTf$^-$, C$_6$H$_5$CO$_2^-$, 4-CH$_3$-C$_6$H$_5$S$^-$, and pyridine-*N*-oxide, showed the opposite trend, in which the *stronger* Lewis base X correlated with a slower rate of decomposition.[54] These data were rationalized via a mechanism of decay involving homolytic Fe-O bond cleavage to give Fe^{II}, which would be destabilized by electron-donating ligands.

For our own system we considered four possible decay pathways (eqs 1 - 4):

$$Fe^{III} - OOR \rightarrow Fe^{IV}(O) + \cdot OR \tag{1}$$

$$Fe^{III} - OOR \rightarrow Fe^{II} + \cdot OOR \tag{2}$$

$$Fe^{III} - OOR \rightarrow Fe^{V}(O) + {}^{-}OR \tag{3}$$

$$Fe^{III} - OOR \rightarrow Fe^{III} + {}^{-}OOR \tag{4}$$

The first pathway, eq 1, is seen for the previously mentioned low-spin Fe^{III}-OOR species, but is unlikely for **1a– 3a** and **1b – 3b** because we do not observe the rise of a peak between 700 – 900 nm that is characteristic of an $Fe^{IV}(O)$ complex. In addition, the lack of any evidence of oxygen-atom-transfer or hydrogen-atom abstraction chemistry during the decomposition of these species in the presence of substrates such as PPh_3 or CHD strongly argues against the generation of an $Fe^{IV}(O)$ complex. Homolytic cleavage of the Fe-O bond would give Fe^{II} (eq 2) as described for the high-spin Fe^{III}-OOR species, but in this case the trend in decomposition rates versus the nature of the thiolate donor should be reversed. Thus our data support either eq 3 or eq 4 as the likely mechanism of decay for **1a – 3a** and **1b – 3b**. In eq 3, heterolytic O-O bond cleavage gives an $Fe^{V}(O)$ complex. We have seen no spectroscopic evidence for the production of an $Fe^{V}(O)$ complex, although such a species may be too short-lived to be observed. However, it is expected that an $Fe^{V}(O)$ species would be a powerful oxidant, and should react rapidly with exogenous substrates such as PPh_3 or cyclooctene. The observed lack of reactivity with these substrates argues against the generation of an $Fe^{V}(O)$ species. The mechanism of decay in eq 4 involves heterolytic Fe-O bond cleavage, releasing the alkylperoxide ligand as either an anion ($^-$OOR), or perhaps as the protonated hydroperoxide (HOOR) with proton donation from exogenous H_2O or ROH. This mechanism is consistent with the kinetic data, and matches nicely with trends in the Fe-O bond lengths from EXAFS. The longer, and therefore weaker, Fe-O bonds should favor enhanced decomposition via this mechanism. Thus we suggest that these thiolate-ligated Fe^{III}-OOR complexes decay via release of ROOH, in analogy to the mechanism for SOR. However, the final fates of the alkyperoxo ligands or the iron complexes are not known at this time. We previously examined the decay products by EPR spectroscopy, but did not observe any new high-spin or low-spin Fe^{III} species.[26] Therefore the initial iron decay product may decompose rapidly to EPR-silent species. More studies are warranted to probe further details of the decay mechanism.

Summary and Conclusions

The alkylperoxo-iron(III) complexes **1a** – **3a** were characterized by XAS studies and compared with their iron(II) precursors. The XANES spectra reveal edge positions that correspond to Fe^{II} for **1 – 3** and Fe^{III} for **1a – 3a**, and pre-edge features for **1a** and **2a** are consistent with conversion from 5- to 6-coordinate upon going from Fe^{II} to Fe^{III}, although for **3a** changes in the pre-edge features are more complex. Analysis of the EXAFS spectra show that **1a** – **3a** are 6-coordinate, and confirm the first coordination sphere is comprised of N_4SO ligation. These data provide the first direct structural characterization of these metastable species. The EXAFS-derived bond lengths reveal that the Fe-O bonds in thiolate-ligated **1a** – **3a** are significantly elongated compared to other low-spin Fe^{III}-OOR complexes that do not contain thiolate ligands. In addition, there is a subtle trend observed for the Fe-O bond distances versus identity of the thiolate donor, in which the Fe-O bond shortens as the thiolate donor becomes less electron-rich. This trend is in agreement both with the vibrational data from RR spectroscopy and with the optimized geometries obtained from DFT.

The reactivity of the alkylperoxo-iron(III) complexes was examined with various substrates. It was shown that the alkylperoxo complexes are not competent electrophilic oxidants, failing to react with the nucleophilic substrates PPh_3 or cyclooctene. In contrast, addition of electrophilic substrates such as aldehydes or H^+ greatly accelerated the rate of decay of the alkylperoxo species. This observation suggests that the alkylperoxo species function as nucleophilic oxidants, in concert with the nucleophilic behavior of other metal-peroxo complexes.[51][53] These studies also suggest that thiolate-ligated **1a** – **3a** do not decompose via O-O bond cleavage to give high-valent iron-oxo species. These results contrast previous work on non-thiolate-ligated, low-spin, alkylperoxo-iron(III) complexes, which decompose

via homolytic O-O bond cleavage to give $Fe^{IV}(O)$ complexes.[40,48,49] Furthermore, an increase in the electron-releasing nature of the thiolate ligands in **1a** – **3a** correlates with faster rates of decay for these species, in agreement with a weakening of the Fe-O bond as seen by RR and now EXAFS studies, and supported by DFT. Taken together with the substrate reactivity, these studies suggest that the thiolate-ligated alkylperoxo-iron(III) complexes decompose via a mechanism dominated by Fe-O, and not O-O, bond cleavage, and this decay pathway may be facilitated by the presence of the thiolate donors. These results are interesting in light of the proposals for the mechanism of SOR, which must release H_2O_2 via Fe-O bond cleavage and avoid O-O cleavage. Some evidence suggests that an Fe^{III}-OO(H) intermediate in SOR should be high-spin, including recent DFT calculations, 55 and the high-spin state may help to favor release of H_2O_2. 28 However, definitive evidence regarding the structure and spin-state of peroxo intermediate(s) in the native reaction of SOR with superoxide remains to be obtained. The active site structure of SOR may be carefully tuned by the choice of ligands (His_4Cys), and in particular the presence of the thiolate donor, to favor Fe-O over O-O cleavage, producing H_2O_2 instead of a high-valent Fe(O) species.

Synopsis

A series of metastable alkylperoxo-iron(III) complexes of formula $[Fe^{III}([15]aneN_4)(SAr)(OOR)]^+$, together with their iron(II) precursors, were characterized by X-ray absorption spectroscopy (XAS). The electronic properties of the arylthiolate donor are systematically varied within this $[N_4S]Fe$ donor set, and are seen to effect both the structure and reactivity of the Fe^{III}-OOR intermediates. These results are described in the context of the potential role of the unusual cysteinate donor in the active site of superoxide reductase.
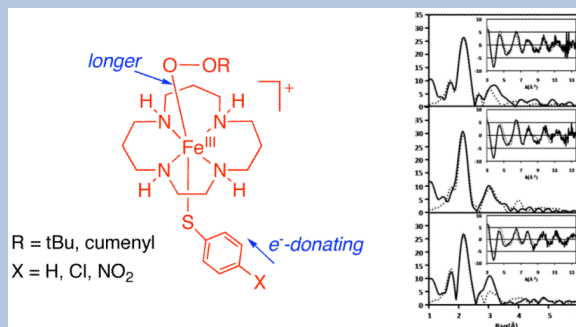
Supplementary Material

Refer to Web version on PubMed Central for supplementary material.

Acknowledgments

References

(1). Emerson JP, Coulter ED, Cabelli DE, Phillips RS, Kurtz DM Jr. Biochemistry. 2002; 41:4348–4357. [PubMed: 11914081]

(2). Katona G, Carpentier P, Nivière V, Amara P, Adam V, Ohana J, Tsanov N, Bourgeois D. Science. 2007; 316:449–453. [PubMed: 17446401]

(3). Kurtz DM Jr. Acc. Chem. Res. 2004; 37:902–908. [PubMed: 15612680]

(4). Lombard M, Houée-Levin C, Touati D, Fontecave M, Nivière V. Biochemistry. 2001; 40:5032–5040. [PubMed: 11305919]

(5). Mathé C, Weill CO, Mattioli TA, Berthomieu C, Houée-Levin C, Tremey E, Nivière V. J. Biol. Chem. 2007; 282:22207–22216. [PubMed: 17545670]

(6). Nivière V, Lombard M, Fontecave M, Houée-Levin C. FEBS Lett. 2001; 497:171–173. [PubMed: 11377434]

(7). Horner O, Mouesca JM, Oddou JL, Jeandey C, Nivière V, Mattioli TA, Mathé C, Fontecave M, Maldivi P, Bonville P, Halfen JA, Latour JM. Biochemistry. 2004; 43:8815–8825. [PubMed: 15236590]

(8). Huang VW, Emerson JP, Kurtz DM Jr. Biochemistry. 2007; 46:11342–11351. [PubMed: 17854204]

(9). Mathé C, Mattioli TA, Horner O, Lombard M, Latour JM, Fontecave M, Nivière V. J. Am. Chem. Soc. 2002; 124:4966–4967. [PubMed: 11982354]

(10). Mathé C, Nivière V, Houee-Levin C, Mattioli TA. Biophys. Chem. 2006; 119:38–48. [PubMed: 16084640]

(11). Moura I, Pauleta SR, Moura JJG. J. Biol. Inorg. Chem. 2008; 13:1185–1195. [PubMed: 18719950]

(12). Skrzypczak-Jankun E, Bross RA, Carroll RT, Dunham WR, Funk MO Jr. J. Am. Chem. Soc. 2001; 123:10814–10820. [PubMed: 11686682]

(13). Costas M, Mehn MP, Jensen MP, Que L Jr. Chem. Rev. 2004; 104:939–986. [PubMed: 14871146]

(14). Kovaleva EG, Lipscomb JD. Science. 2007; 316:453–457. [PubMed: 17446402]

(15). Kovaleva EG, Neibergall MB, Chakrabarty S, Lipscomb JD. Acc. Chem. Res. 2007; 40:475–483. [PubMed: 17567087]

(16). Que L Jr. Ho RYN. Chem. Rev. 1996; 96:2607–2624. [PubMed: 11848838]

(17). Rocklin AM, Kato K, Liu HW, Que L Jr. Lipscomb JD. J. Biol. Inorg. Chem. 2004; 9:171–182. [PubMed: 14714198]

(18). Stubbe J, Kozarich JW. Chem. Rev. 1987; 87:1107–1136.

(19). Stubbe J, Kozarich JW, Wu W, Vanderwall DE. Acc. Chem. Res. 1996; 29:322–330.

(20). Skrzypczak-Jankun E, Bross RA, Carroll RT, Dunham WR, Funk MO Jr. J. Am. Chem. Soc. 2001; 123:10814–10820. [PubMed: 11686682]

(21). Karlsson A, Parales JV, Parales RE, Gibson DT, Eklund H, Ramaswamy S. Science. 2003; 299:1039–1042. [PubMed: 12586937]

(22). Shearer J, Scarrow RC, Kovacs JA. J. Am. Chem. Soc. 2002; 124:11709–11717. [PubMed: 12296737]

(23). Bukowski MR, Zhu SR, Koehntop KD, Brennessel WW, Que L Jr. J. Biol. Inorg. Chem. 2004; 9:39–48. [PubMed: 14564557]

(24). Rohde JU, Torelli S, Shan XP, Lim MH, Klinker EJ, Kaizer J, Chen K, Nam WW, Que L Jr. J. Am. Chem. Soc. 2004; 126:16750–16761. [PubMed: 15612713]

(25). Shan X, Rohde JU, Koehntop KD, Zhou Y, Bukowski MR, Costas M, Fujisawa K, Que L Jr. Inorg. Chem. 2007; 46:8410–8417. [PubMed: 17764172]

(26). Krishnamurthy D, Kasper GD, Namuswe F, Kerber WD, Sarjeant AAN, Moënne-Loccoz P, Goldberg DP. J. Am. Chem. Soc. 2006; 128:14222–14223. [PubMed: 17076472]

(27). Namuswe F, Kasper GD, Sarjeant AAN, Hayashi T, Krest CM, Green MT, Moënne-Loccoz P, Goldberg DP. J. Am. Chem. Soc. 2008; 130:14189–14200. [PubMed: 18837497]

(28). Namuswe F, Hayashi T, Jiang YB, Kasper GD, Sarjeant AAN, Moënne-Loccoz P, Goldberg DP. J. Am. Chem. Soc. 2010; 132:157–167. [PubMed: 20000711]

(29). Frisch MJ, et al. Gaussian 03, Revision C.02. 2004

(30). McMaster WH, Del Grande NK, Mallet JH, Hubbell JH. Compilation of X-Ray Cross Sections. 1969 Lawrence Livermore Nat. Lab Rep. UCRL-50174, Sect. 2, Rev. 1.

(31). Weng TC, Waldo GS, Penner-Hahn JE. J. Synchrotron Rad. 2005; 12:506–510.

(32). Binsted N. EXCURV98, CCLRC Daresbury Laboratory computer program. 1998

(33). Dimakis N, Bunker G. Phys. Rev. B. 2002; 65:201103.

(34). Westre TE, Kennepohl P, DeWitt JG, Hedman B, Hodgson KO, Solomon EI. J. Am. Chem. Soc. 1997; 119:6297–6314.

(35). Addison AW, Rao TN, Reedjik J, van Rijn J, Verschoor GC. Dalton Trans. 1984:1349–1456.

(36). Koehntop KD, Rohde JU, Costas M, Que L Jr. Dalton Trans. 2004:3191–3198. [PubMed: 15483700]

(37). Lehnert N, Ho RYN, Que L Jr. Solomon EI. J. Am. Chem. Soc. 2001; 123:8271–8290. [PubMed: 11516278]

(38). Lehnert N, Neese F, Ho RYN, Que L Jr. Solomon EI. J. Am. Chem. Soc. 2002; 124:10810–10822. [PubMed: 12207537]

(39). Bautz J, Comba P, Que L Jr. Inorg. Chem. 2006; 45:7077–7082. [PubMed: 16933906]

(40). Jensen MP, Costas M, Ho RYN, Kaizer J, Payeras AMI, Münck E, Que L Jr. Rohde JU, Stubna A. J. Am. Chem. Soc. 2005; 127:10512–10525. [PubMed: 16045338]

(41). Roelfes G, Vrajmasu V, Chen K, Ho RYN, Rohde JU, Zondervan C, la Crois RM, Schudde EP, Lutz M, Spek AL, Hage R, Feringa BL, Münck E, Que L Jr. Inorg. Chem. 2003; 42:2639–2653. [PubMed: 12691572]

(42). Roe AL, Schneider DJ, Mayer RJ, Pyrz JW, Widom J, Que L Jr. J. Am. Chem. Soc. 1984; 106:1676–1681.

(43). Neese F. J. Biol. Inorg. Chem. 2006; 11:702–711. [PubMed: 16821037]

(44). Lehnert N, Fujisawa K, Solomon EI. Inorg. Chem. 2003; 42:469–481. [PubMed: 12693229]

(45). Lehnert N, Ho RYN, Que L Jr. Solomon EI. J. Am. Chem. Soc. 2001; 123:12802–12816. [PubMed: 11749538]

(46). Seo MS, Kamachi T, Kouno T, Murata K, Park MJ, Yoshizawa K, Nam W. Angew. Chem., Int. Ed. 2007; 46:2291–2294.

(47). Park MJ, Lee J, Suh Y, Kim J, Nam W. J. Am. Chem. Soc. 2006; 128:2630–2634. [PubMed: 16492048]

(48). Jensen MP, Payeras AMI, Fiedler AT, Costas M, Kaizer J, Stubna A, Münck E, Que L Jr. Inorg. Chem. 2007; 46:2398–2408. [PubMed: 17326618]

(49). Kaizer J, Costas M, Que L Jr. Angew. Chem., Int. Ed. 2003; 42:3671–3673.

(50). Sobolev AP, Babushkin DE, Talsi EP. J. Mol. Catal. A. 2000; 159:233–245.

(51). Wertz DL, Valentine JS. Struct. Bonding. 2000; 97:37–60.

(52). Annaraj J, Suh Y, Seo MS, Kim SO, Nam W. Chem. Commun. 2005:4529–4531.

(53). Hikichi S, Okuda H, Ohzu Y, Akita M. Angew. Chem., Int. Ed. 2009; 48:188–191.

(54). Bukowski MR, Halfen HL, van den Berg TA, Halfen JA, Que L Jr. Angew. Chem., Int. Ed. 2005; 44:584–587.

(55). Surawatanawong P, Tye JW, Hall MB. Inorg. Chem. 2010; 49:188–198. [PubMed: 19968237]
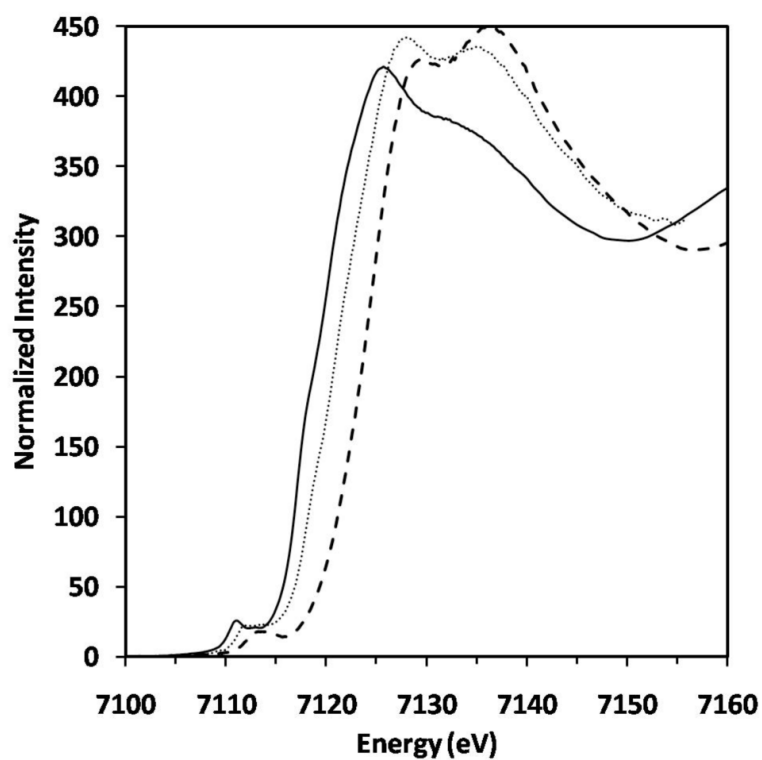
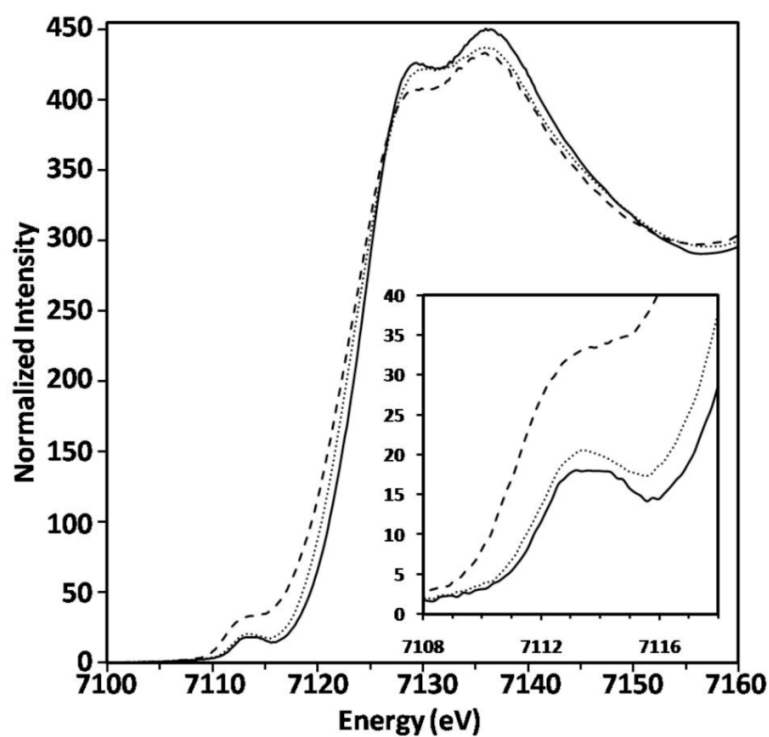**Figure 1.**
Normalized Fe K-Edge XANES of [Fe^{II}([15]aneN$_4$)(SC$_6$H$_5$)]BF$_4$ (**1**) as a crystalline solid dispersed in BN matrix (−) and dissolved in CH$_2$Cl$_2$ (···), and [Fe^{III}([15]aneN$_4$)(SC$_6$H$_5$)(OOtBu)]BF$_4$ (**1a**) (---) dissolved in CH$_2$Cl$_2$.
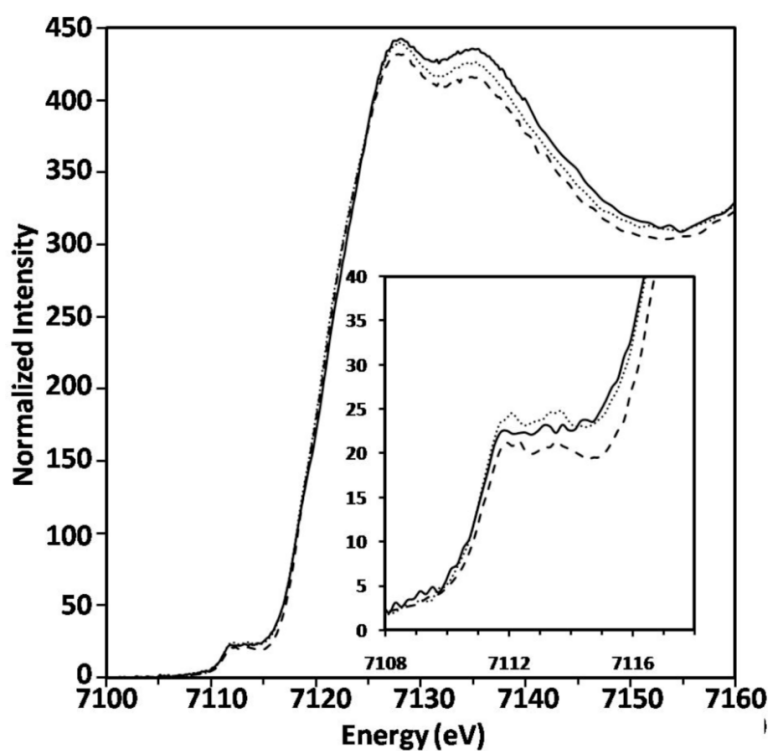
Figure 2.
Normalized Fe K-Edge XANES in CH_2Cl_2 of $[Fe^{II}([15]aneN_4)(SC_6H_5)]BF_4$ (**1**) (−),
$[Fe^{II}([15]aneN_4)(SC_6H_4$-$p$-Cl)]BF_4$ (**2**) (···), and $[Fe^{II}([15]aneN_4)(SC_6H_4$-$p$-NO_2)]BF_4$ (**3**)
(---). Inset: expanded view of pre-edge features.

Figure 3.
Normalized Fe K-Edge XANES in CH_2Cl_2 of $[Fe^{III}([15]aneN_4)(SC_6H_5)(OOtBu)]BF_4$ (**1a**) (−), $[Fe^{III}([15]aneN_4)(SC_6H_4\text{-}p\text{-}Cl)(OOtBu)]BF_4$ (**2a**) (···), and $[Fe^{III}([15]aneN_4)(SC_6H_4\text{-}p\text{-}NO_2)(OOtBu)]BF_4$ (**3a**) (---). Inset: expanded view of pre-edge features.
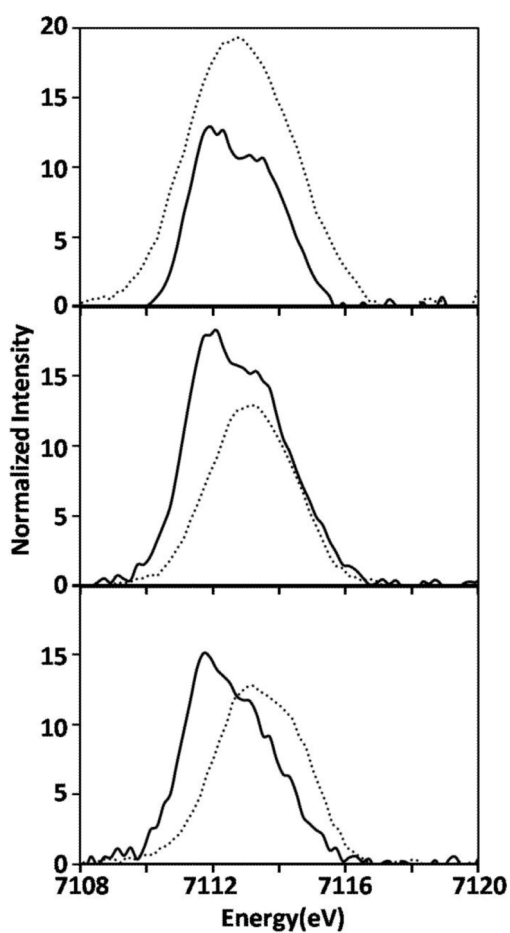
Figure 4.
Background-subtracted pre-edge features for (bottom) [Fe^{II}([15]aneN$_4$)(SC$_6$H$_5$)]BF$_4$ (**1**) (−)
and [Fe^{III}([15]aneN$_4$)(SC$_6$H$_5$)(OOtBu)]BF$_4$ (**1a**) (···), (middle) [Fe ([15]aneN$_4$)(SC$_6$H$_4$-*p*-Cl)]BF$_4$ (**2**) (−) and [Fe^{III}([15]aneN$_4$)(SC$_6$H$_4$-*p*-Cl)(OOtBu)]BF$_4$ (**2a**) (···), and (top)
[Fe^{II}([15]aneN$_4$)(SC$_6$H$_4$-*p*-NO$_2$)]BF$_4$ (**3**) (−) and [Fe^{III}([15]aneN$_4$)(SC$_6$H$_4$-*p*-NO$_2$)
(OOtBu)]BF$_4$ (**3a**) (···).
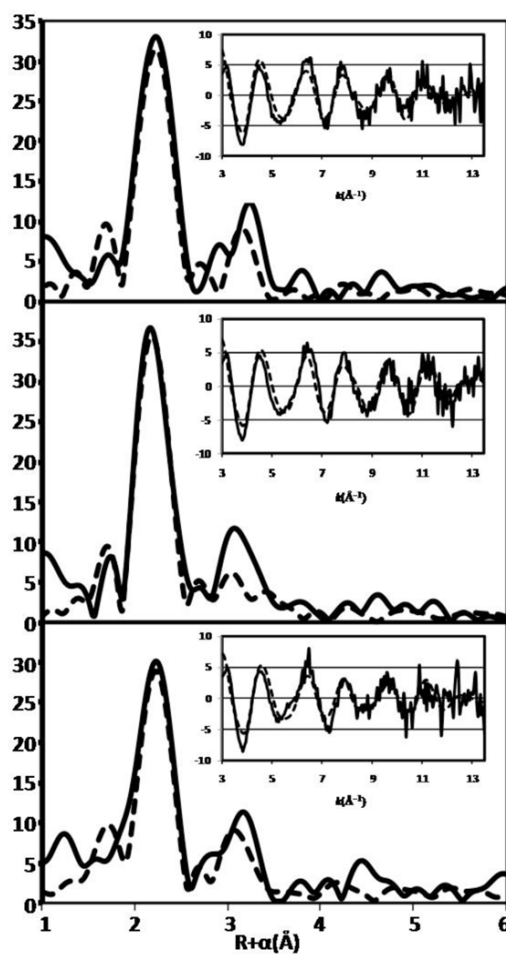
Figure 5.
Fourier transforms of Fe K-edge EXAFS data and EXAFS spectra (insets) in CH_2Cl_2, experimental data (—) and theoretical fits (⋯) for (bottom) $[Fe^{II}([15]aneN_4)(SC_6H_5)]BF_4$ (**1**), (middle) $[Fe^{II}([15]aneN_4)(SC_6H_4\text{-}p\text{-Cl})]BF_4$ (**2**), and (top) $[Fe^{II}([15]aneN_4)(SC_6H_4\text{-}p\text{-}NO_2)]BF_4$ (**3**).
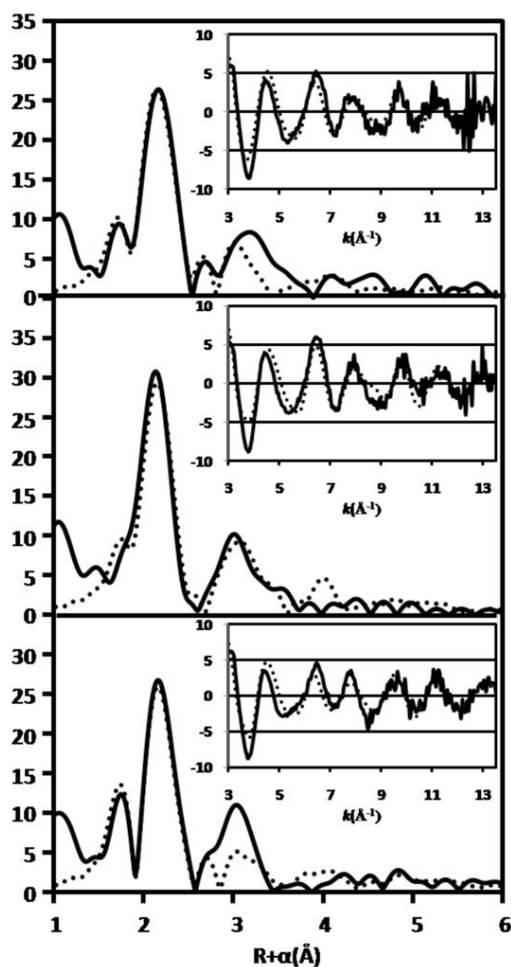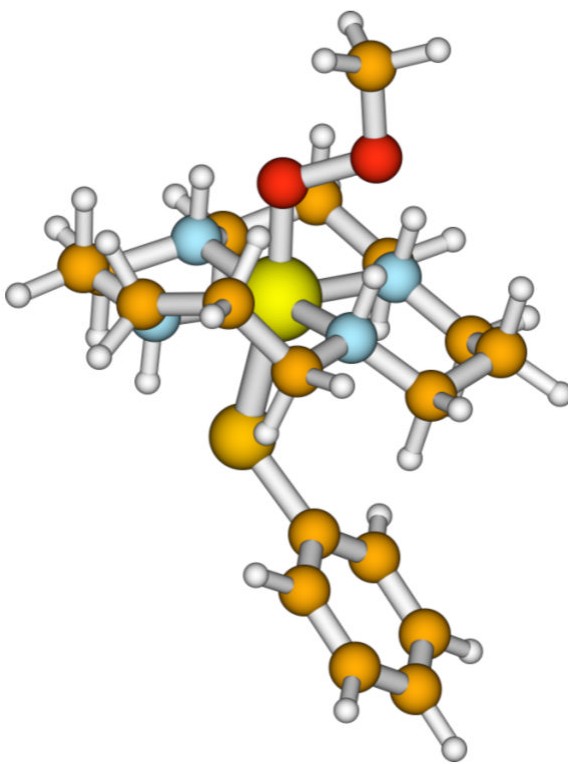
Figure 6.
Fourier transforms of Fe K-edge EXAFS data and EXAFS spectra (insets) in CH_2Cl_2, experimental data (—) and theoretical fits (⋯) for (bottom) [Fe^{III}([15]aneN$_4$)(SC$_6$H$_5$) (OOtBu)]BF$_4$ (**1a**), (middle) [Fe^{III}([15]aneN$_4$)(SC$_6$H$_4$-*p*-Cl)(OOtBu)]BF$_4$ (**2a**), and (top) [Fe^{III}([15]aneN$_4$)(SC$_6$H$_4$-*p*-NO$_2$)(OOtBu)]BF$_4$ (**3a**).

Figure 7.
Molecular structure of [Fe^{III}([15]aneN$_4$)(SPh)(OOMe)]$^+$ based on the optimized geometry from DFT (yellow, Fe; red, O; orange, C; grey, H).
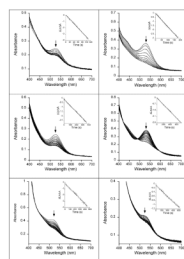
Figure 8.
Time-resolved UV-visible spectra for the decay of [Fe^{III}([15]aneN$_4$)(SC$_6$H$_4$-*p*-X)(OOtBu)]BF$_4$ (**1a**, 1.9 mM; **2a**, 1.9 mM; **3a**, 1.4 mM) (left) and [Fe^{III}([15]aneN$_4$)(SC$_6$H$_4$-*p*-X)(OOCm)]BF$_4$ (**1b**, 2.6 mM; **2b**, 2.0 mM; **3b**, 1.3 mM) (right). From top to bottom, X = H, Cl, NO$_2$. Inset: plot of ln[(A$_t$-A$_f$)/(A$_0$-A$_f$) vs time (open circles), and the best fit of the data (black line), giving slope = k_{dec}.
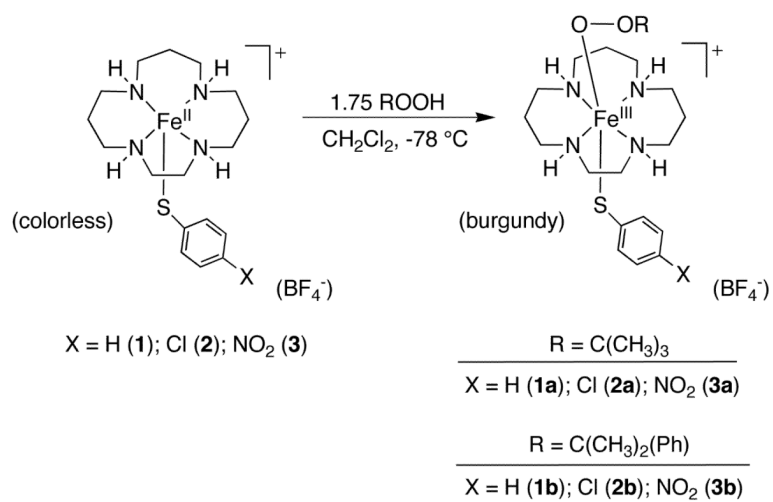
Scheme 1.
Formation of Fe^{III}–OOR Complexes at −78 °C
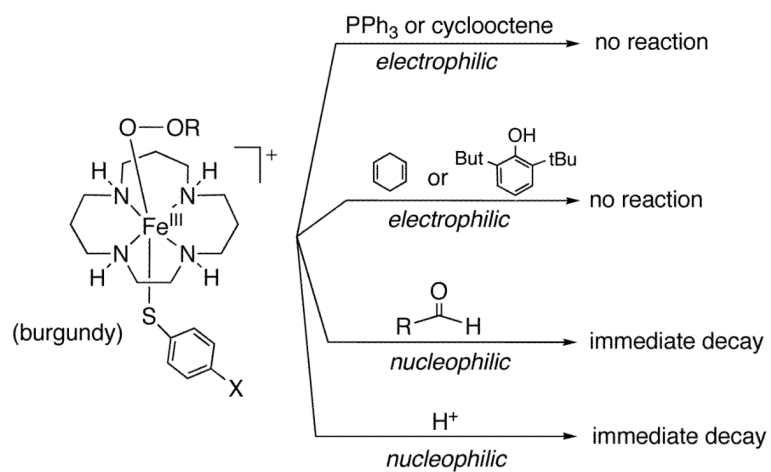
Scheme 2.
Reactivity Pattern of Thiolate-ligated Fe^{III}-OOR Complexes

Table 1

Least-squares Fits of the EXAFS Data[a] for the Iron(II) complexes **1** – **3** in CH_2Cl_2

Complex	Fit	Coord no.	R_{ab} (Å)[b]	σ^{2c}	Coord no.	R_{ab} (Å)[b]	σ^{2c}	Coord no.	R_{ab} (Å)[b]	σ^{2c}	E_0	F^d
1	1	4N	2.00	2.0	8C	2.93	3.0	3C	3.27	5.0	−8.93	2.13
	2	1S	2.31	2.0	1C	3.43	3.0	2C	4.16	5.0	−6.93	1.64
		4N	2.01	4.0	8C	2.96	10.0	3C	3.26	8.0		
	3	**1S**	**2.31**	**2.8**	**1C**	**3.43**	**10.2**	**2C**	**4.16**	**12.3**	**−6.93**	**1.60**
		4N	**2.01**	**4.8**	**8C**	**2.96**	**12.1**	**3C**	**3.27**	**12.9**		
2	1	4N	2.00	2.0	8C	2.93	3.0	3C	3.28	5.0	−8.95	1.85
	2	1S	2.29	2.0	1C	3.49	3.0	2C	4.22	5.0	−7.14	1.18
		4N	2.02	4.0	8C	2.96	10.0	3C	3.27	8.0		
	3	**1S**	**2.29**	**3.2**	**1C**	**3.49**	**10.1**	**2C**	**4.22**	**11.9**	**−7.14**	**1.08**
		4N	**2.02**	**4.6**	**8C**	**2.96**	**11.9**	**3C**	**3.27**	**13.2**		
3	1	4N	2.00	2.0	8C	2.93	3.0	3C	3.28	5.0	−8.95	2.11
	2	1S	2.31	2.0	1C	3.49	3.0	2C	4.22	5.0	−7.37	1.45
		4N	2.03	4.0	8C	2.97	10.0	3C	3.33	8.0		
	3	**1S**	**2.31**	**3.0**	**1C**	**3.49**	**11.1**	**2C**	**4.22**	**11.9**	**−7.14**	**1.43**
		4N	**2.03**	**4.5**	**8C**	**2.97**	**12.2**	**3C**	**3.33**	**13.0**		

[a] Best fits shown in bold.

[b] Absorber-scatterer distance.

[c] Debye-Waller factor ($Å^2$) × 10^3.

[d] $F = \sum (\chi_{exp} - \chi_{calc})^2 \cdot k^6$. The accuracy in the determination of the bond lengths is approximately 0.02 Å and the precision is 0.004 Å.

Table 2

Least-squares Fits of the EXAFS Data^a for the Iron(III)-OOtBu complexes **1a** – **3a** in CH$_2$Cl$_2$

Complex	Fit	Coord no.	R_{ab} (Å)^b	σ^{2c}	Coord no.	R_{ab}(Å)^b	σ^{2c}	Coord no.	R_{ab}(Å)^b	σ^{2c}	E_0	F^d
1a	1	1 O	1.83	1.0	8 C	3.01	10.0	3 C	3.28	8.0	−11.21	1.66
		4 N	2.07	4.0								
	2	1 S	2.30	2.0	1 C	3.45	3.0	2 C	4.17	5.0	−12.29	1.53
		4 N	2.06	4.0	8 C	3.01	10.0	3 C	3.29	8.0		
	3	2 O	1.87	8.0	8 C	2.97	10.0	3 C	3.30	8.0	−12.65	1.57
		4 N	2.17	4.0								
	4	1 O	1.85	1.0	1 C	3.44	3.0	2 C	4.17	5.0	−10.29	1.44
		1 S	2.30	2.0	8 C	3.01	10.0	3 C	3.28	8.0		
		4 N	2.07	4.0								
	5	0.9 O	1.85	1.0	1 C	3.43	3.0	2 C	4.16	5.0	−10.23	1.41
		0.6 S	2.29	2.0	8 C	3.01	10.0	3 C	3.28	8.0		
		4 N	2.07	4.0								
	6	**0.9 O**	**1.85**	**2.6**	**0.6 C**	**3.43**	**11.3**	**1.2 C**	**4.16**	**14.3**	**−10.23**	**1.41**
		0.6 S	**2.29**	**6.2**	**8 C**	**3.01**	**11.9**	**3 C**	**3.28**	**13.8**		
		4 N	**2.07**	**4.6**								
2a	7	**1 O**	**1.84**	**3.5**	**0.6 C**	**3.40**	**9.6**	**1.2 C**	**4.12**	**12.9**	**−10.61**	**1.63**
		0.6 S	**2.30**	**7.2**	**8 C**	**3.02**	**11.6**	**3 C**	**3.28**	**12.5**		
		4 N	**2.10**	**4.2**								
3a	8	**0.5 O**	**1.82**	**4.1**	**0.6 C**	**3.42**	**10.9**	**1.2 C**	**4.14**	**12.5**	**−9.94**	**1.44**
		0.6 S	**2.32**	**9.0**	**8 C**	**2.96**	**12.3**	**3 C**	**3.27**	**13.3**		
		4 N	**2.06**	**4.0**								

^{a} Best fits shown in bold.

^{b} Absorber-scatterer distance.

^{c} Debye-Waller factor (Å^2) × 10^3.

^{d} $F = \sum (\chi_{exp} - \chi_{calc})^2 \cdot k^6$. The accuracy in the determination of the bond lengths is approximately 0.02 Å and the precision is 0.004 Å.

Table 3

Comparison of Bond Distances for **1a - 3a** from EXAFS and DFT (B3LYP/6311G)

Complex	Fe-N (Å)		Fe-S (Å)		Fe-O (Å)		
	EXAFS	DFT	EXAFS	DFT	EXAFS	DFT	ν(Fe-O) cm^{-1}
1a	2.07	2.09	2.29	2.374	1.85	1.873	611
2a	2.10	2.09	2.30	2.380	1.84	1.870	612
3a	2.06	2.09	2.32	2.388	1.82	1.864	615